Biosensors and Bioelectronics 167 (2020) 112477

Contents lists available at ScienceDirect

Biosensors and Bioelectronics

journal homepage: http://www.elsevier.com/locate/bios

Oxygen vacancies enhanced photoelectrochemical aptasensing of 2, 3', 5, 5'-tetrachlorobiphenyl amplified with Ag_3VO_4 nanoparticle-TiO_2 nanotube array heterostructure

Si Zhang [a], Hejie Zheng [a], Yuping Sun [a], Fen Li [a], Tongtong Li [a], Xiaoqiang Liu [a,*], Yanmei Zhou [a], Weiwei Chen [b], Huangxian Ju [b,**]

[a] Henan Joint International Research Laboratory of Environmental Pollution Control Materials, College of Chemistry and Chemical Engineering, Henan University, Kaifeng, 475004, PR China

[b] State Key Laboratory of Analytical Chemistry for Life Science, College of Chemistry and Chemical Engineering, Nanjing University, Nanjing, 210023, PR China

ARTICLE INFO

Keywords:
Photoelectrochemical aptasensing
Signal amplification
Ag_3VO_4 nanoparticles
Oxygen vacancies
TiO_2 nanotube arrays
Resonance energy transfer

ABSTRACT

This work proposed an enhancing mechanism of both oxygen vacancies (OVs) and the heterostructure for amplifying the photoelectrochemical (PEC) aptasensing signal. The OVs were formed by *in situ* electrochemical reduction of TiO_2 nanotube arrays (TNTAs), and well-separated Ag_3VO_4 nanoparticles (NPs) were then deposited on the TNTAs. The band gaps and positions of these nanomaterials were evaluated by Tauc equation and Mott-Schottky plots to verify the formation of the heterojunction. The OVs and heterojunction greatly enhanced the visible light absorption and improved the charge separation of TNTAs. The amplified PEC signal could be quenched by the resonance energy transfer between Ag_3VO_4 NPs and gold nanorods (Au NRs), which were labeled on the complementary DNA (cDNA) to the aptamer immobilized on the heterojunction. Upon the recognition of the aptamer to target analyte, the Au NR-cDNA was detached from the sensor, leading to a "signal-on" aptasensing strategy. Under optimal conditions, the PEC aptasensor displayed a detection limit of 0.015 pg mL^{-1} and a linear range from 0.02 to 300 ng mL^{-1} for 2,3',5,5'-tetrachlorobiphenyl.

1. Introduction

Photoelectrochemical (PEC) technique, which combines photochemistry with electrochemical methods (Yan et al., 2015a), has displayed several advantages of high signal-noise ratio, rapid detection and stable signal (Lei et al., 2016; Qiu et al., 2019; Shu and Tang, 2017; Tang et al., 2019). However, the sensitivity of PEC detection has not been significantly improved compared with its electrochemical counterpart (Feng et al., 2018; Liu et al., 2018; Wang et al. 2018b, 2018c). Therefore, several signal amplification strategies including steric hindrance effects (Zhao et al., 2012), enzymatic reactions (Wang et al., 2010; Zhao et al., 2013), sensitization effects (Fan et al., 2014), resonance energy transfer (RET) (Wang et al., 2018a) were applied for improving the sensitivity of PEC sensors. In addition, different modification methods of photoactive materials including doping, introduction of oxygen vacancies (OVs), formation of heterojunction and Z-scheme were also used to enhance the PEC signals (Xing et al., 2017; Xiu et al., 2018; Yang et al., 2019).

TiO_2 is one type of the most extensively used photosensitive materials in PEC sensing due to their high photo-electrical conversion capability, stability and excellent biocompatibility (Kong et al., 2019; Ni et al., 2007; Roy et al., 2011; Sun et al., 2018). Particularly, TiO_2 nanotube arrays (TNTAs) displayed enhanced electron transportation rate and higher PEC efficiency than other TiO_2 materials because of its one-dimensional structure, uniform and vertical alignment, and its intimate contact with Ti foil substrate (Tian et al., 2019; Liu et al., 2011; Xiang et al., 2018). Nevertheless, the inherent big band gap (~3.2eV) and the easy photo-generated charge recombination of TiO_2 led to its poor utilization of solar energy and relatively low photocatalytic efficiency (Cai et al., 2017; Zhang et al., 2018).

As a common type of defect, oxygen vacancies can produce a new defect level in TiO_2 to narrow the band gap and improve the visible light absorption (Pan et al., 2013; Wang et al., 2019). They can also act as the capture centers for photogenerated electrons to reduce the recombination of electron-hole pairs. Furthermore, OVs are regarded as the

* Corresponding author.
** Corresponding author.
E-mail addresses: liuxq@henu.edu.cn (X. Liu), hxju@nju.edu.cn (H. Ju).

https://doi.org/10.1016/j.bios.2020.112477
Received 6 June 2020; Received in revised form 14 July 2020; Accepted 25 July 2020
Available online 7 August 2020

shallow donors (charge carriers) to enhance the carrier density, which thus increased the conductivity of TiO_2 (Jiao et al., 2017; Xu et al., 2015). Many methods such as high temperature treatment (Lv et al., 2013), sodium borohydride reduction (Kang et al., 2013), plasma bombardment (Kimmel and Petrik, 2008), combustion (Zuo et al., 2010), *etc.* have been used to generate OVs. To circumvent the complex conditions and expensive equipment required by the above techniques, this work employed a simple and facile electrochemical reduction method for producing OVs on TNTAs. In addition, the formation of a heterostructure with a narrow band gap nanomaterial also effectively improved the PEC performance of TNTAs (Zheng et al., 2020).

In this work, Ag_3VO_4 nanoparticles (Ag_3VO_4 NPs) were deposited on OV-TNTAs to form a heterojunction of Ag_3VO_4|OV-TNTAs on a Ti foil electrode. The narrow band gap of Ag_3VO_4 NPs (~2.2 eV) facilitated the visible light absorption of TNTAs, meanwhile the severe aggregation of Ag_3VO_4 NPs was greatly relieved after the formation of the heterojunction. Using 2,3',5,5'-tetrachlorobiphenyl (PCB72) as the analyte model, an ultrasensitive aptasensor was designed by immobilizing PCB72 aptamer on Ag_3VO_4|OV-TNTAs electrode. The amplified PEC signal could be quenched by the RET between Ag_3VO_4 NPs and Au NR-cDNA hybridized with the aptamer on the aptasensor, leading to a "signal-on" PEC response upon the recognition of the aptamer to PCB72. The heterojunction, OVs and RET effect contributed to the excellent performance of the PEC aptasensor.

2. Experimental section

2.1. Material and reagents

The chemicals and materials are presented in S1.1 of the Supporting information. The PCB72 aptamer and corresponding complementary DNA were synthesized and purified by Shanghai Sangon Biotechnology Co., Ltd (Shanghai, China). Their sequences were given below:

PCB72 aptamer: 5′-NH_2-$(CH_2)_6$-CACTC GGACC CCATT CTCCT TCCAT CCCTC ATCCG TCCAC-3′

Complementary DNA (cDNA): 5′-SH-$(CH_2)_6$-TTTTT GGACG GATGA GGGAT-3′

2.2. Apparatus

The instruments used in this work are presented in S1.2 of the Supporting information.

2.3. Fabrication of OV-TNTAs

TNTAs were prepared via the typical electrochemical anodization method. The Ti foil was firstly diced into 1 cm × 3.5 cm pieces, and placed in a mixed acid solution (HF: HNO_3: H_2O = 2 : 8: 12) for 10 min to remove the surface oxides and other impurities. Afterward, the diced Ti foil pieces were sequentially cleaned with toluene, acetone, ethanol and ultrapure water for 15 min each in an ultrasonic cleaner. The anodization was carried out in a mixed electrolyte solution (NH_4F (0.82414 g), ethylene glycol (80 mL) and ultrapure water (9 mL)) at a constant potential of 50 V on a two-electrode system with the Ti foil as the working electrode and a platinum wire as the counter electrode for 5 h. Afterward, the asprepared TNTAs were immediately washed with absolute ethanol and dried in air. Finally the amorphous TNTAs were annealed at 450 °C for 3 h with a temperature escalating rate of 4 °C min^{-1}.

OV-TNTAs were prepared by electrochemically reducing TNTAs in a two-electrode cell using TNTAs and a Pt electrode as the cathode and anode, respectively. A voltage of 5 V was applied on TNTAs for 35 s in 1.0 M Na_2SO_4 solution. After that, OV-TNTAs were ultrasonically washed with ultrapure water to remove the residual Na_2SO_4.

2.4. Preparation of Ag_3VO_4|TNTAs and Ag_3VO_4|OV-TNTAs heterojunction

Firstly, 0.2 mmol $NaVO_3$ (30 mL) solution was dropwise added into 40 mL of $AgNO_3$ aqueous solution (0.6 mmol) under stirring for 10 min. After that, the mixed solution was adjusted with 4 M NaOH solution to pH 11.0, followed by vigorous stirring for 5 h at room temperature. Subsequently, the above solution and asprepared TNTAs or OV-TNTAs were transferred into a 100-mL Teflon-lined stainless autoclave, remained at 140 °C for 8 h and then cooled down to room temperature. The obtained Ag_3VO_4|TNTAs and 0.20-Ag_3VO_4|OV-TNTAs (0.20 represents the molar ratio of Ag_3VO_4 NPs to TNTAs) were thoroughly washed with ultrapure water and dried at 60 °C. Similarly, pristine Ag_3VO_4 NPs and the other Ag_3VO_4|OV-TNTAs with different ratios of Ag_3VO_4 NPs were synthesized with the same procedures.

2.5. Preparation of Au NRs and Au NR-cDNA conjugates

The synthesis of Au NRs followed the seed-mediated growth method with minor modification (Wu et al., 2017), as presented in S1.3 of the Supporting information.

Thiolated cDNA was conjugated to Au NRs via the Au–S bonding. Firstly, a mixed solution of 15 μL of 10 mM TCEP and 30 μL of 50 μM HS-cDNA was incubated for 30 min at room temperature to activate HS-cDNA. Following that, a certain amount of Au NRs was added into the above solution and the obtained dispersion was gently shaken for 16 h in a dark environment. The unbound cDNA was removed by 10 min centrifugation and the prepared Au NR-cDNA was stored in 0.1 M PBS (pH 7.0, 0.1 M KCl).

2.6. Fabrication of the aptasensor and detection of PCB72

A droplet of 30 μL (1% w/v) chitosan was applied on an Ag_3VO_4|OV-TNTAs electrode (1 × 3.5 cm^2). The electrode was then immersed in PBS (0.02 M, pH 7.4) containing 2 mg mL^{-1} BS^3 for 1 h. Afterward, 30 μL of 3.0 μM aptamer was immobilized on the electrode and incubated overnight at 4 °C, and the modified electrode was then washed with PBS to remove unbound aptamer. After that, the aptamer modified electrode was blocked by 3% (w/v) BSA for 1 h, and was washed again with PBS. Subsequently, 30 μL of Au NR-cDNA was applied on the electrode to obtain the aptasensor, which was thoroughly cleaned with PBS and stored at 4 °C. Prior to the detection, the aptasensors were incubated with PCB72 solutions (30 μL) with different concentrations at 37 °C for 1 h. All the PEC measurements were conducted in 0.1 M PBS (pH 7.4, 0.1 M KCl) at a potential of 0.2 V using a 300 W Xe lamp as the visibleight source with a 420 nm cut-off filter, which was switched on and off at an interval of 30 s during the test.

3. Results and discussion

3.1. Verification of the formation of Ag_3VO_4|OV-TNTAs

The SEM morphologies of TNTAs, OV-TNTAs, Ag_3VO_4 NPs, Ag_3VO_4|OV-TNTAs and Au NRs are shown in Fig. 1. The top and cross-sectional (inset) views of pure TNTAs (Fig. 1A) display that homogeneous and vertically aligned TNTAs were perfectly grown on the Ti template with a uniform pore diameter of ~100 nm and an average length of ~6 μm. For comparison, the magnified SEM images of both pristine TNTAs (left) and OV-TNTAs (right) are displayed in Fig. 1B, which indicates that the morphology of TNTAs remains unchanged after the introduction of OVs. As shown in Fig. 1C, pristine Ag_3VO_4 NPs were seriously self-aggregated into bulky and irregular lumps in the absence of other nanomaterials. Fig. 1D and 1E demonstrate that a large amount of scattered nanoparticles have been deposited on TNTA tubes without obvious aggregation, indicating that the Ag_3VO_4|OV-TNTAs heterojunction was successfully formed. In addition, Au NRs with an average length of ~50

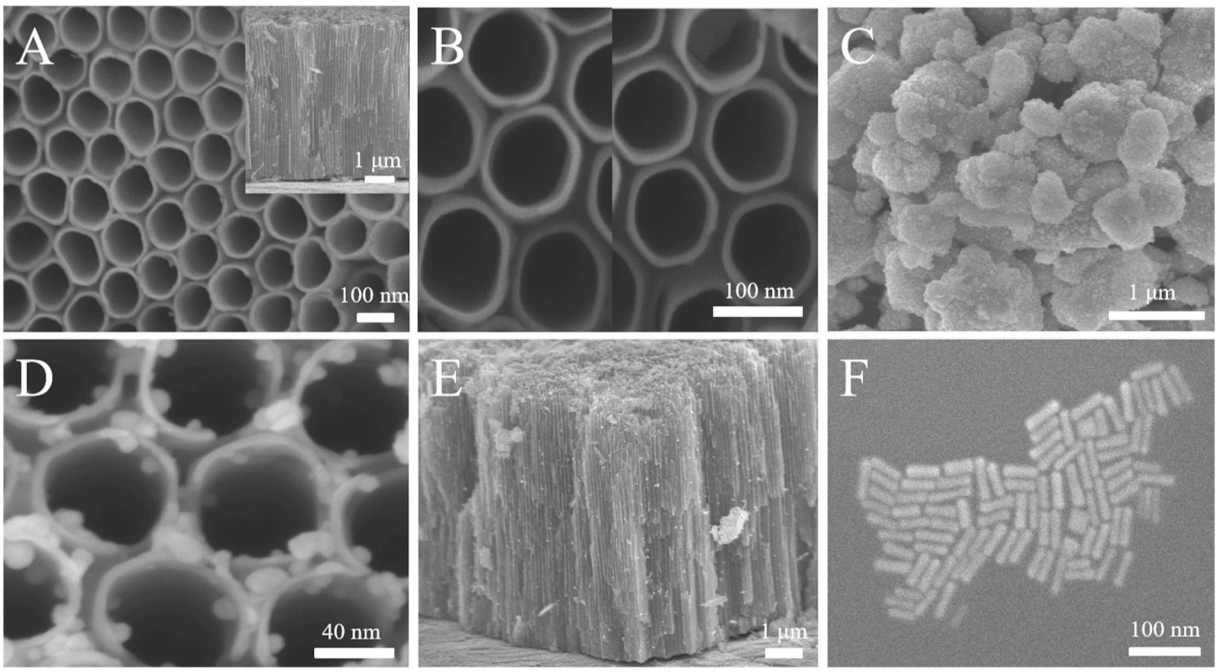

Fig. 1. SEM images of (A) top view of TNTAs (inset: partial cross-sectional view), (B) top views of TNTAs (left) and OV-TNTAs (right), (C) Ag_3VO_4 NPs, (D) top view of Ag_3VO_4|OV-TNTAs, (E) partial cross-sectional view of Ag_3VO_4|OV-TNTAs and (F) Au NRs.

nm were also prepared for RET amplification, as shown in Fig. 1F.

EPR spectra of TNTAs and OV-TNTAs were obtained to verify the existence of OVs and Ti^{3+} defects on TNTAs. Both TNTAs and OV-TNTAs (Fig. 2A) display obvious EPR signals at a g value of ~2.003, mainly because the unpaired electrons were trapped by OVs on both materials (Xiao et al., 2018). In particular, OV-TNTAs exhibit much stronger intensity than TNTAs, indicating the significant increase of OVs caused by the electrochemical reduction treatment. In addition, another strong signal at a g value of ~1.97 is assigned to Ti^{3+} defects in OV-TNTAs (Zuo et al., 2012), which was produced by the reduction of Ti^{4+} ions.

The XPS spectra were collected to investigate the surface chemical composition and elemental valence of Ag_3VO_4|OV-TNTAs. Firstly, all the typical element peaks (Ti, O, Ag, V and C) of Ag_3VO_4|OV-TNTAs were observed on the survey scan spectrum (Fig. 2B). The high-resolution spectra of Ti 2p (Fig. 2C) were deconvoluted into four peaks: the two peaks at 458.6 and 464.1 eV are ascribed to Ti^{3+} $2p_{3/2}$

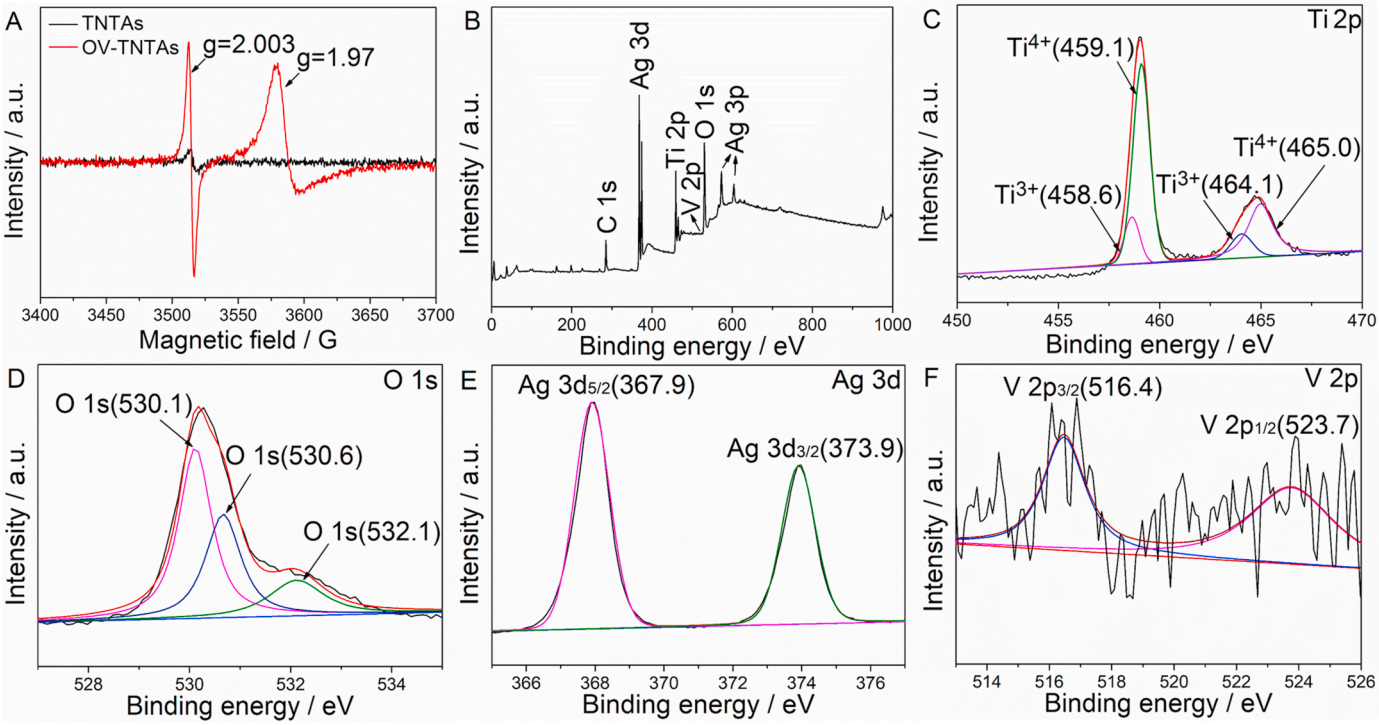

Fig. 2. (A) EPR spectra of TNTAs and OV-TNTAs, (B) XPS survey spectrum and high-resolution (C) Ti 2p, (D) O 1s, (E) Ag 3d and (F) V 2p XPS spectra of Ag_3VO_4|OV-TNTAs.

and Ti^{3+} $2p_{1/2}$, and the other two peaks at 459.1 and 465.0 eV correspond to Ti^{4+} $2p_{3/2}$ and Ti^{4+} $2p_{1/2}$, clearly indicating the presence of Ti^{3+} species on Ag_3VO_4|OV-TNTAs (Tan et al., 2018). In addition, the high-resolution O 1s spectrum could be deconvoluted into three peaks at 530.1, 530.6 and 532.1 eV (Fig. 2D), attributed to O^{2-} in the V–O bond of Ag_3VO_4 NPs, O^{2-} in the TNTAs lattice, and –OH adsorbed on the sample surface, respectively (Pan et al., 2018). The high-resolution spectrum of Ag 3d exhibits two peaks at 367.9 and 373.9 eV, ascribed to Ag $3d_{5/2}$ and Ag $3d_{3/2}$, respectively (Fig. 2E), confirming the existence of Ag^+ rather than metal Ag in the heterojunction (Le et al., 2019). The V 2p peaks of Ag_3VO_4 NPs at 516.4 and 523.7 eV could be ascribed to V $2p_{3/2}$ and V $2p_{1/2}$ (Fig. 2F), which confirmed the presence of V^{5+} (Zhang et al., 2013). In summary, the above XPS analysis supports the successful preparation of Ag_3VO_4|OV-TNTAs.

Furthermore, the formation of Ag_3VO_4|OV-TNTAs can also be verified by XRD, which shows several diffraction peaks at 25.3°, 37.8°, 48.0°, 53.8° and 55.0° (Fig. 3A, curve a) corresponding to (101), (004), (200), (105) and (211) crystalline planes of anatase TNTAs (JCPDS No. 21–1272), respectively (Li et al., 2014). The other undesignated diffraction peaks on this curve were assigned to metal Ti (JCPDS No. 41–1049) (Ma et al., 2018). The XRD patterns of TNTAs (curve a) and OV-TNTAs (curve b) were almost identical, which revealed that the crystal form of OV-TNTAs was not changed after the introduction of OVs. On curve c, the peaks at 19.2°, 30.9°, 32.3°, 34.2°, 35.1°, 35.9°, 38.9°, 51.1° and 54.1° were ascribed to the (011), (−121), (121), (220), (301), (202), (022), (132) and (331) planes of monoclinic Ag_3VO_4 (JCPDS No. 43–0542), respectively (Wang et al., 2014). Most importantly, a characteristic diffraction peak at 32.3° assigned to the (121) crystal plane of Ag_3VO_4 NPs and almost all the TNTAs peaks are observed on curve d, indicating the formation of Ag_3VO_4|OV-TNTAs.

3.2. Optical properties of the prepared nanomaterials

The formation of the heterojunction and OVs could promote the photogenerated charge separation, which was confirmed by the Photoluminescence (PL) spectra under 355-nm excitation (Fig. 3B). It is known that the recombination of electron-hole pairs can generate PL peaks and their intensity is inversely proportional to the separation efficiency of charge carriers (Zhao et al., 2018). As expected, TNTAs displaythe largest PL intensity among all the materials, implying the fastest recombination of photogenerated charges. The PL intensity of Ag_3VO_4|TNTAs is obviously smaller than that of TNTAs, indicating that the formation of heterojunction retarded the recombination of photogenerated charges. The introduction of OVs on TNTAs effectively facilitated the separation of electron-hole pairs, resulting in further decrease of PL intensity, which is even smaller than that of Ag_3VO_4|TNTAs. Furthermore, Ag_3VO_4|OV-TNTAs display the smallest PL intensity among all the materials due to the formation of the heterojunction and OVs.

The optical absorption properties of the prepared nanomaterials were also evaluated with UV-DRS, as shown in Fig. 3C. The absorption edge of pure TNTAs is located at ~390 nm (curve a), indicating its sole absorption in the ultraviolet region. Compared with the pure TNTAs, OV-TNTAs (curve b) display much stronger visible light absorption (~400–800 nm) because the OVs could produce a localized state below the conduction band (CB) to narrow the band gap of TNTAs. The absorption edge of pure Ag_3VO_4 NPs (curve c) is located at ~587 nm in the visible light region. As expected, Ag_3VO_4|OV-TNTAs (curve d) exhibit intensive absorption in both UV and visible light regions due to the formation of heterojunction and OVs. The above results indicated the feasibility of using Ag_3VO_4|OV-TNTAs as a visible light photoelectrode in PEC biosensors.

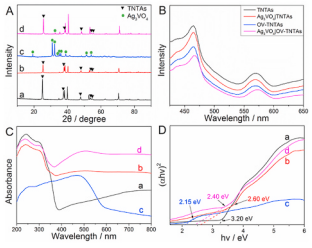

Fig. 3. (A) XRD patterns of (a) TNTAs, (b) OV-TNTAs, (c) Ag_3VO_4 NPs and (d) Ag_3VO_4|OV-TNTAs, (B) PL emission spectra of TNTAs, OV-TNTAs, Ag_3VO_4|TNTAs, Ag_3VO_4|OV-TNTAs, (C) DRS spectra and (D) Tauc plots obtained from DRS spectra of (a) TNTAs, (b) OV-TNTAs, (c) Ag_3VO_4 NPs and (d) Ag_3VO_4|OV-TNTAs.

3.3. Calculation of band gaps and positions

The band gaps of different prepared nanomaterials were obtained by Tauc equation: $\alpha h\nu = A(h\nu\text{-}E_g)^{n/2}$, where α, h, ν, A and E_g represent the absorption coefficient, Planck constant, incident light frequency, a constant and band gap energy, respectively. Based on the plots of $(\alpha h\nu)^2$ versus (hν) (Fig. 3D) obtained from the UV-DRS spectra (Fig. 3C), the energy band gaps of TNTAs (curve a), OV-TNTAs (curve b), Ag_3VO_4 NPs (curve c) and Ag_3VO_4|OV-TNTAs (curve d) were estimated to be ~3.20, 2.60, 2.15 and 2.40 eV, respectively. Next, the valence band-edge energy (E_{VB}) of Ag_3VO_4 NPs was evaluated by the formula of $E_{VB} = X - E^e + 0.5E_g$, where X (5.645) is the electronegativity of Ag_3VO_4 obtained from the previous publication (Zhao et al., 2019), E_g is the band gap of the semiconductor, and E^e (4.5 eV) represents the energy of free electrons in the hydrogen scale. Accordingly, the E_{VB} value of Ag_3VO_4 NPs was calculated to be ~2.22 eV, and a E_{CB} value of ~0.07 eV was obtained based on $E_{CB} = E_{VB} - E_g$.

The energy band positions of OV-TNTAs were obtained using electrochemical Mott-Schottky test (Fig. 4A). By extrapolating the linear part of the Mott-Schottky plots to the X axis, the flat band potentials of TNTAs and OV-TNTAs were estimated to be −0.4 and −0.63 V (vs Ag|AgCl), and their E_{CB} were obtained as −0.2 and −0.43 V (vs NHE) respectively after being corrected with Ag|AgCl electrode. Based on $E_{VB} = E_{CB} + E_g$, the E_{VB} values of TNTAs and OV-TNTAs were calculated to be 3.0 and 2.17 V (vs NHE), respectively.

3.4. PEC and EIS characterization for aptasensor assembling

The assembly process of the PEC aptasensor was presented in Scheme 1 and the transient photocurrents were recorded in Fig. 4B under intermittent visible light irradiation to verify this process. TNTAs (curve a) only generated a small photocurrent due to its poor visible light absorption and the rapid recombination of electron-hole pairs. After the electrochemical reduction treatment, the photocurrent was increased by ~96% (curve b) owing to the introduction of OVs into TNTAs, which enhanced the absorption of visible light and suppressed the recombination of electron-hole pairs. Compared with that of OV-TNTAs, the photocurrent of Ag_3VO_4|TNTAs (curve c) was further increased by ~53% due to the formation of the heterojunction, which effectively promoted the separation of electron-hole pairs and absorption of visible light. As expected, Ag_3VO_4|OV-TNTAs (curve d) produced the largest photocurrent among all the modified electrodes, attributed to the synergistic effect from OVs and heterojunction. Subsequently, the immobilization of PCB72 aptamer on Ag_3VO_4|OV-TNTAs resulted in a significant decrease of photocurrent owing to the steric hindrance effect (curve e). As expected, the introduction of Au NR-cDNA on aptamer|Ag_3VO_4|OV-TNTAs led to a terrific decrease (~67%) of the photocurrent (curve f), which should be attributed to the RET effect between Au NRs and Ag_3VO_4 NPs. Eventually, the photocurrent recovered (curve g) after the addition of PCB72, which specifically bound with the aptamer to detach Au NR-cDNA from the electrode surface, and minimized the RET effect.

To further confirm the sequential assembly of the aptasensor, EIS

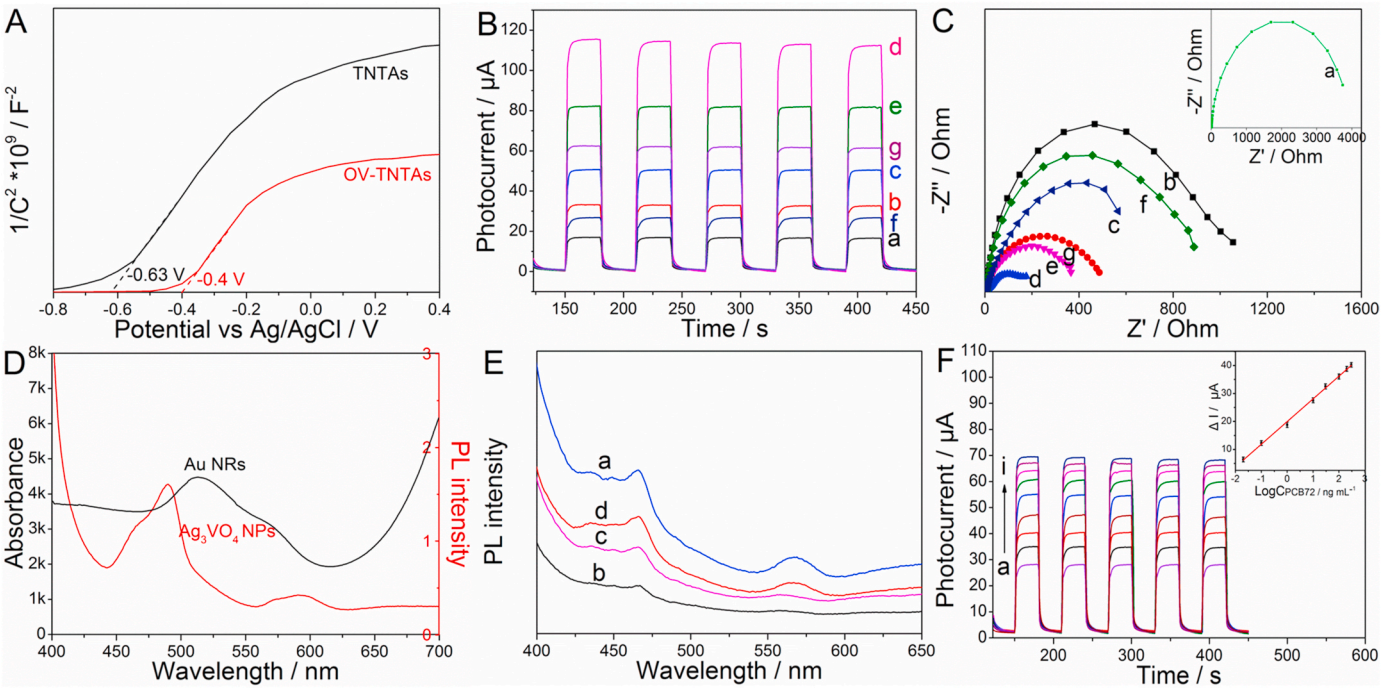

Fig. 4. (A) Mott-Schottky plots of TNTAs and OV-TNTAs, (B) Photocurrents at 0.2 V in 0.1 M PBS (pH 7.4) under 420 nm irradiation, (C) Nyquist plots of 5 mM $[Fe(CN)_6]^{3-/4-}$ in 0.1 M KCl at (a) TNTAs, (b) OV-TNTAs, (c) Ag_3VO_4|TNTAs, (d) Ag_3VO_4|OV-TNTAs, (e) aptamer|Ag_3VO_4|OV-TNTAs, (f) Au NR-cDNA|aptamer|Ag_3VO_4|OV-TNTAs and (g) PCB72|Au NR-cDNA|Ag_3VO_4|OV-TNTAs, (D) UV–Vis absorption spectrum of Au NRs and PL emission spectrum of Ag_3VO_4 NPs, (E) PL emission spectra of (a) aptamer|Ag_3VO_4|OV-TNTAs, (b) Au NR-cDNA|aptamer|Ag_3VO_4|OV-TNTAs and after introduction of (c) 1.0 ng mL^{-1} and (d) 10 ng mL^{-1} of PCB72 on Au NR-cDNA|aptamer|Ag_3VO_4|OV-TNTAs, (F) Photocurrent responses to (a–i) 0, 0.02, 0.1, 1.0, 10, 30, 100, 200, 300 ng mL^{-1} PCB72, Inset: corresponding linear calibration curve.

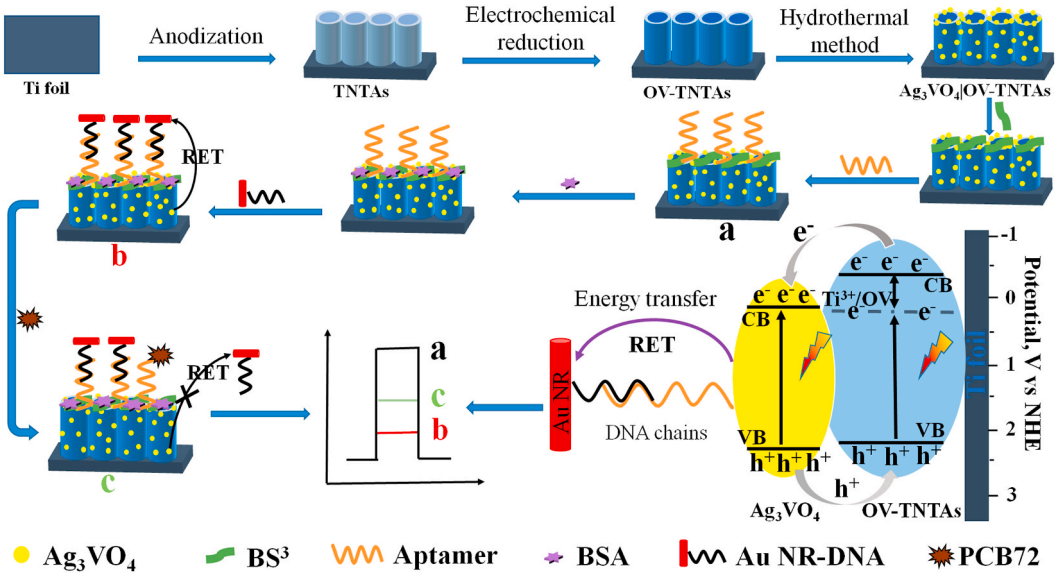

Scheme 1. Schematic diagram for the construction and mechanism of the PEC aptasensor.

measurements were performed to collect the Nyquist plots of 5 mM $[Fe(CN)_6]^{3-/4-}$ in 0.1 M KCl at different assembling stages. The arc diameter of Nyquist plot was proportional to the electron transfer resistance (*R*et) at the electrode/electrolyte interface (Zhang et al., 2014). As shown in Fig. 4C, the *R*et values at both OV-TNTAs (curve b) and Ag_3VO_4|TNTAs (curve c) are much smaller than that at TNTAs (curve a), implying that both OVs and the heterojunction greatly increased the carrier density and improved the charge transport. Especially, Ag_3VO_4|OV-TNTAs (curve d) show the smallest Ret among all the electrodes, attributed to the synergistic effect from OVs and the heterojunction. After the aptamer was immobilized on Ag_3VO_4|OV-TNTAs (curve e), the Ret was remarkably increased owning to the steric hindrance effect of bio-moleclues. Further increase of the Ret was observed after the electrode was modified with Au NR-cDNA (curve f). Eventually, the introduction of PCB72 (curve g) largely diminished the Ret because Au NR-cDNA was removed from the electrode surface by PCB72 with higher affinity to the aptamer. In summary, both transient photocurrents and impedance measurements proved the successful assembly of the PEC aptasensor.

3.5. Feasibility of RET effect and working mechanism of aptasensing

Besides the formation of OVs and heterojunction, the RET effect could also enhance the sensitivity of the aptasensor. The emission spectrum of Ag_3VO_4 NPs and the absorption spectrum of Au NRs should be overlapped to produce the RET effect (Zeng et al., 2013). As shown in Fig. 4D, the absorption band of Au NRs with a peak at ~512 nm is mostly overlapped with the PL emission peak of Ag_3VO_4 NPs at ~490 nm, indicating the highly possible existence of the RET between the two materials. Furthermore, the PL spectra of the modified electrodes at different assembly stages were collected to verify the RET between Ag_3VO_4 NPs and Au NRs. In Fig. 4E, the aptamer|Ag_3VO_4|OV-TNTAs electrode possesses the strongest fluorescence band (curve a), which was then quenched by Au NR-cDNA due to the RET effect (curve b). After PCB72 analyte at the concentrations of 1.0 and 10 ng mL^{-1} was successively applied, the fluorescence intensities of Au NR-cDNA|aptamer|Ag_3VO_4|OV-TNTAs gradually recovered (curves c and d) because the binding between PCB72 and aptamer detached Au NR-cDNA from the electrode surface, which stepwise weakened the RET effect with the increasing PCB72 concentrations. All the above results indicated the feasibility of RET for PEC detection of PCB72.

Based on the above experimental results including the band positions of OV-TNTAs and Ag_3VO_4 NPs estimated by the theoretical calculation, the electron transfer process of Ag_3VO_4|OV-TNTAs and the possible mechanism of the PEC aptasensor was proposed in Scheme 1. Due to the well matching band positions between OV-TNTAs and Ag_3VO_4 NPs, the two semiconductors perfectly formed a heterojunction, which reduced the photogenerated charge recombination and band gap of OV-TNTAs. Furthermore, the OVs produced a defect energy level under the CB of OV-TNTAs to not only narrow the band gap of TNTAs, but also trap the photogenerated electrons for promoting the charge separation.

Firstly, both OV-TNTAs and Ag_3VO_4 NPs in the heterojunction could readily absorb visible light to transit electrons from valence band (VB) of Ag_3VO_4 NPs to its CB and from VB of OV-TNTAs via the defect energy level to its CB. Because the CB and VB levels of OV-TNTAs are higher than the corresponding band levels of Ag_3VO_4 NPs, the photo-generated electrons then transferred from the CB of OV-TNTAs to that of Ag_3VO_4 NPs, and the holes on the VB of Ag_3VO_4 NPs moved to that of OV-TNTAs. The directed movement of the photogenerated charges would greatly improve the separation of photogenerated electron-hole pairs and therefore enhanced the PEC performance of the aptasensor.

Next, the photocurrent could be quenched by the RET between Ag_3VO_4 NPs and Au NR-cDNA, which was hybridized with the aptamer on the heterojunction. Due to the RET effect, the excitation energy on the heterojunction was transferred to Au NRs due to the surface plasmon resonance, which facilitated the recombination of electron-hole pairs and thus decreased the photocurrent. The subsequent introduction of PCB72 destroyed the hybridization between the aptamer and Au NR-cDNA due to the high affinity of PCB72 to the aptamer, which weakened the RET and thus restored the photocurrent for "signal-on" biosensing.

3.6. Optimization of experimental parameters and PEC detection of PCB72

Various experimental parameters including loading amount of aptamer, incubation time of PCB72, pH of the test solution, the applied potential and molar ratio in Ag_3VO_4|OV-TNTAs were optimized. The photocurrent at Ag_3VO_4|OV-TNTAs gradually decreased until the aptamer concentration arrives at 3.0 μM, then tended to be stable (Fig. S1A), probably due to the saturated immobilization of aptamer on the electrode. Therefore, 3.0 μM was chosen as the optimal concentration of aptamer. After 10 ng mL^{-1} PCB72 was incubated on the aptasensor, the photocurrent increased with the increasing incubation time and flattened after ~60 min (Fig. S1B), likely owing to the thorough completion of the specific binding between the aptamer and PCB72. The photocurrent at the aptasensor increased with the increasing pH of the test solution, and reached a maximum value at pH 7.4 (Fig. S1C). Consequently, the optimum incubation time of 60 min and pH of 7.4 were used in the following PEC detection. The photocurrent increased rapidly with the increasing applied potential from 0 V to 0.2 V and then enhanced slowly (Fig. S1D) due to the promoted separation of electron-hole pairs. A low bias potential of 0.2 V was selected to minimize the possible interference from the detection solution. In addition, the ratio of Ag_3VO_4 NPs to OV-TNTAs in the heterojunction was also optimized (Fig. S1E). When the molar ratio was over 0.2, the photocurrent slightly decreased mainly due to the excessive loading of Ag_3VO_4 NPs, which may aggregate to hinder the transfer of electrons.

Under the optimum conditions, the photocurrent increased proportionally with the increase of PCB72 concentration (Fig. 4F). The plot of ΔI vs the logarithm of PCB72 concentration ranging from 0.02 to 300 ng mL^{-1} shows a good linearity, where ΔI is defined as the photocurrent change in the absence (I_0) and presence (I) of the PCB72 (the inset of Fig. 4F). The regression equation is expressed as $\Delta I = (19.9 \pm 0.905) + (8.11 \pm 0.209) \times \mathrm{Log}\ (C_{PCB72}/\mathrm{ng\ mL^{-1}})$ (μA) (all errors represent 95% confidence intervals using Student's t-test), with a correlation coefficient of 0.996. Furthermore, the detection limit (LOD) was calculated to be 0.015 pg mL^{-1} with a signal-to-noise ratio of 3. Compared with the previous reports (Xu et al., 2012; Zhai et al., 2013; Yan, Z. et al., 2015b; Lin et al., 2016a; Lin et al., 2016b; Liu et al., 2019) in Table S1, the proposed aptasensor shows the apparent superiority in linear range and detection limit due to the special features of the heterojunction, oxygen vacancy defects and RET effect.

3.7. Stability, specificity, reproducibility and practical application of PEC aptasensor

The photocurrent remained stable after 5 off-on-off irradiation cycles (Fig. 4F), demonstrating the short-term stability of the aptasensor. Meanwhile, the photocurrent still retained 97.1% ± 2.9%, 93.3% ± 4.3% and 89.5% ± 4.76% of its initial value at the 95% confidence intervals ($n = 4$) after storing the aptasensor for 1 weeks, 2 weeks and 4 weeks at 4 °C respectively, indicating the excellent long-term storage stability. The specificity of the proposed aptasensor was also evaluated by detecting PCB72 in the presence of the possible coexisting interferences (Fig. S1F). Although the concentrations of interferences are much higher than that of target PCB72, the photocurrent change caused by target PCB72 was at least ~4.5 times higher than that by the interferences, due to the high specific affinity of the aptamer for PCB72. Additionally, the reproducibility of the aptasensor was studied by the interassay test, and the relative standard deviation (RSD) of the test was used to evaluate the results. At PCB72 concentrations of 0.02, 0.1 and 1.0 ng mL^{-1}, RSD values of 2.51%, 3.27%, and 3.49% were respectively obtained under the same experimental conditions using four identical electrodes, indicating the acceptable reproducibility of the PEC aptasensor for PCB72 assay.

The practical applicability of the aptasensors was also assessed in both lake water and tap water using the standard addition method. PCB72 at concentrations of 1.0, 50.0 and 100.0 ng mL^{-1} were added into the water samples, the recoveries obtained by both the aptasensors and the routine HPLC were compared in Table 1 to verify the accuracy and reliability of the proposed aptasensors. The two methods show the similar recoveries from 93.0% to 103.2% at different concentrations, indicating the practical application prospect of the aptasensor. In addition, this aptasensor shows superiority of simple instrument, fast detection, less cost and easy operation over HPLC.

4. Conclusions

An ultrasensitive "signal-on" PEC aptasensor for PCB72 detection has been developed with a designed signal enhancing mechanism using Ag_3VO_4|OV-TNTAs as the photosensitive material. The introduction of

Table 1
Detection of PCB72 in different water samples with the PEC aptasensor ($n = 4$).

Sample		PEC aptasensor			HPLC		
	Add (ng mL^{-1})	Found[a] (ng mL^{-1})	Recovery (%)	SD[b] (ng mL^{-1})	Found[a] (ng mL^{-1})	Recovery (%)	SD[b] (ng mL^{-1})
Lake water	0	Undetected			Undetected		
	1	0.94	94.0	0.082	0.97	97.0	0.061
	50	50.1	100.2	0.296	50.3	100.6	0.323
	100	103.2	103.2	1.978	99.7	99.7	1.745
Tap water	0	Undetected			Undetected		
	1	0.93	93.0	0.071	0.94	94.0	0.068
	50	48.7	97.4	0.189	49.2	98.4	0.156
	100	103.1	103.1	1.816	99.6	99.6	1.634

[a] All uncertainties represent the 95% confidence intervals.
[b] Standard deviation.

OVs and the formation of the heterojunction with separated Ag_3VO_4 NPs have been confirmed by various characterization techniques and theory calculation. The heterojunction promoted visible light absorption and photogenerated charge separation, which greatly enhanced the PEC signal. Besides, the RET effect between Ag_3VO_4 and Au NR-cDNA also contributed to the excellent performance for detection of PCB72. The aptasensor exhibited a wide linear range, a low detection limit, excellent stability, specificity and reproducibility. The proposed PEC amplification mechanism would be used to construct the biosensors for practical biological, medical and environmental analysis.

CRediT authorship contribution statement

Si Zhang: Conceptualization, Methodology, Investigation, Writing - original draft, Software. **Hejie Zheng:** Investigation. **Yuping Sun:** Visualization. **Fen Li:** Software. **Tongtong Li:** Validation. **Xiaoqiang Liu:** Conceptualization, Methodology, Funding acquisition, Writing - original draft. **Yanmei Zhou:** Supervision. **Weiwei Chen:** Investigation. **Huangxian Ju:** Methodology, Writing - review & editing, Supervision.

Declaration of competing interest

The authors declare that they have not known competing financial interests or personal relationships that could have appeared to influence the work reported in this paper.

Acknowledgements

This work was financially supported by National Natural Science Foundation of China (No. U1504215, 21576071, 21776061), International Science and Technology Cooperative Project funded by The Department of Science and Technology of Henan Province (172102410042), the program for Science & Technology Innovation Talents in Universities of Henan Province (19HASTIT037) and the program for Science & Technology Innovation Team in Universities of Henan Province (19IRTSTHN029).

Appendix A. Supplementary data

Supplementary data to this article can be found online at https://doi.org/10.1016/j.bios.2020.112477.

References

Cai, J., Huang, J., Ge, M., Iocozzia, J., Lin, Z., Zhang, K.Q., Lai, Y., 2017. Small 13, 1604240.
Fan, G.C., Ren, X.L., Zhu, C., Zhang, J.R., Zhu, J.J., 2014. Biosens. Bioelectron. 59, 45–53.
Feng, J., Li, Y., Gao, Z., Lv, H., Zhang, X., Fan, D., Wei, Q., 2018. Biosens. Bioelectron. 99, 14–20.
Jiao, X., Chen, Z., Li, X., Sun, Y., Gao, S., Yan, W., Wang, C., Zhang, Q., Lin, Y., Luo, Y., Xie, Y., 2017. J. Am. Chem. Soc. 139, 7586–7594.
Kang, Q., Cao, J., Zhang, Y., Liu, L., Xu, H., Ye, J., 2013. J. Mater. Chem. A 1, 5766.
Kimmel, G.A., Petrik, N.G., 2008. Phys. Rev. Lett. 100, 196102.
Kong, W., Li, Q., Xia, L., Li, X., Sun, H., Kong, R.-M., Qu, F., 2019. Microchim. Acta 186, 490.
Le, S., Li, W., Li, Y., Borjigin, B., Li, G., Wang, X., 2019. Photochem. Photobiol. 95, 501–511.
Lei, K.J., Lin, Y.M., Ren, J., Bai, L., Miao, Y.C., An, G.Y., Song, C.P., 2016. Plant Cell Physiol. 57, 192–203.
Li, H., Chen, Z., Tsang, C.K., Li, Z., Ran, X., Lee, C., Nie, B., Zheng, L., Hung, T., Lu, J., Pan, B., Li, Y.Y., 2014. J. Mater. Chem. A 2, 229–236.
Lin, S., Gan, N., Cao, Y., Chen, Y., Jiang, Q., 2016a. J. Chromatogr. A 1446, 34–40.
Lin, S., Gan, N., Zhang, J., Qiao, L., Chen, Y., Cao, Y., 2016b. Talanta 149, 266–274.
Liu, C., Teng, Y., Liu, R., Luo, S., Tang, Y., Chen, L., Cai, Q., 2011. Carbon 49, 5312–5320.
Liu, S., Chen, Q., Wang, Z., Cao, T., Zhao, G., Zhou, Y., 2019. Analyst 144, 4841–4847.
Liu, X.P., Chen, J.S., Mao, C.J., Niu, H.L., Song, J.M., Jin, B.K., 2018. Biosens. Bioelectron. 116, 23–29.
Lv, Y., Pan, C., Ma, X., Zong, R., Bai, X., Zhu, Y., 2013. Appl. Catal., B 138–139, 26–32.
Ma, Y., Wang, N., Chen, J., Chen, C., San, H., Chen, J., Cheng, Z., 2018. ACS Appl. Mater. Interfaces 10, 22174–22181.
Ni, M., Leung, M.K.H., Leung, D.Y.C., Sumathy, K., 2007. Renew. Sustain. Energy Rev. 11, 401–425.
Pan, J., You, M., Chi, C., Dong, Z., Wang, B., Zhu, M., Zhao, W., Song, C., Zheng, Y., Li, C., 2018. Int. J. Hydrogen Energy 43, 6586–6593.
Pan, X., Yang, M.Q., Fu, X., Zhang, N., Xu, Y.J., 2013. Nanoscale 5, 3601–3614.
Qiu, Z., Shu, J., Liu, J., Tang, D., 2019. Anal. Chem. 91, 1260–1268.
Roy, P., Berger, S., Schmuki, P., 2011. Angew. Chem. Int. Ed. 50, 2904–2939.
Shu, J., Tang, D., 2017. Chem. Asian J. 12, 2780–2789.
Sun, D., Zhang, W., Lin, Y., Liu, Z., Shen, W., Zhou, L., Rao, X., Liu, S., Cai, X.-a., He, D., Fu, S., 2018. For. Ecol. Manage 422, 1–10.
Tan, S., Xing, Z., Zhang, J., Li, Z., Wu, X., Cui, J., Kuang, J., Zhu, Q., Zhou, W., 2018. J. Catal. 357, 90–99.
Tang, J., Xiong, P., Cheng, Y., Chen, Y., Peng, S., Zhu, Z.Q., 2019. Biosens. Bioelectron. 130, 125–131.
Tian, H., Chen, K., Ye, X., Yang, S., Gu, Q., 2019. Ceram. Int. 45, 20750–20757.
Wang, J., Liang, H., Zhang, C., Jin, B., Men, Y., 2019. Appl. Catal., B 256, 117874.
Wang, P., Du, Y., Li, Y., Ren, D., Song, C.P., 2010. Plant Cell 22, 2981–2998.
Wang, S., Hun, X., Luo, X., 2018a. Sens. Actuators, B 260, 388–395.
Wang, S., Li, D., Sun, C., Yang, S., Guan, Y., He, H., 2014. Appl. Catal., B 144, 885–892.
Wang, Y., Wang, P., Wu, Y., Di, J., 2018b. Sens. Actuators, B 254, 910–915.
Wang, Y., Zhang, L., Cui, K., Xu, C., Li, H., Liu, H., Yu, J., 2018c. Nanoscale 10, 3421–3428.
Wu, L., Ding, F., Yin, W., Ma, J., Wang, B., Nie, A., Han, H., 2017. Anal. Chem. 89, 7578–7585.
Xiang, S., Zhang, Z., Wu, Z., Sun, L., Radjenovic, P., Ren, H., Lin, C., Tian, Z., Li, J., 2018. ACS Appl. Energy Mater. 2, 558–568.
Xiao, L., Liu, T., Zhang, M., Li, Q., Yang, J., 2018. ACS Sustain. Chem. Eng. 7, 2483–2491.
Xing, X., Zhang, M., Hou, L., Xiao, L., Li, Q., Yang, J., 2017. Int. J. Hydrogen Energy 42, 28434–28444.
Xiu, Z., Xing, Z., Li, Z., Wu, X., Yan, X., Hu, M., Cao, Y., Yang, S., Zhou, W., 2018. Mater. Res. Bull. 100, 191–197.
Xu, Q., Yu, J., Zhang, J., Zhang, J., Liu, G., 2015. Chem. Commun. 51, 7950–7953.
Xu, S.M., Yuan, H., Chen, S.P., Xu, A., Wang, J., Wu, L.J., 2012. Anal. Biochem. 423, 195–201.
Yan, K., Liu, Y., Yang, Y., Zhang, J., 2015a. Anal. Chem. 87, 12215–12220.
Yan, Z., Gan, N., Wang, D., Cao, Y., Chen, M., Li, T., Chen, Y., 2015b. Biosens. Bioelectron. 74, 718–724.
Yang, Y., Wu, Y., Ma, L., Yang, Z., Dong, Q., Li, Q., Ni, X., Kudla, J., Song, C., Guo, Y., 2019. Plant Cell 31, 1367–1384.
Zeng, X., Ma, S., Bao, J., Tu, W., Dai, Z., 2013. Anal. Chem. 85, 11720–11724.
Zhai, G.S., Wu, X.N., Lehmler, H.J., Schnoor, J.L., 2013. Chem. Cent. J. 7, 183.
Zhang, L., He, Y., Ye, P., Qin, W., Wu, Y., Wu, T., 2013. Mater. Sci. Eng. B 178, 45–52.

Zhang, Z., Jing, W., Tan, X., Yu, T., Ma, J., 2018. J. Mater. Sci. 53, 6170–6182.
Zhang, Z., Yang, X., Hedhili, M.N., Ahmed, E., Shi, L., Wang, P., 2014. ACS Appl. Mater. Interfaces 6, 691–696.
Zhao, T., Xing, Z., Xiu, Z., Li, Z., Shen, L., Cao, Y., Hu, M., Yang, S., Zhou, W., 2018. Mater. Res. Bull. 103, 114–121.
Zhao, W., Feng, Y., Huang, H., Zhou, P., Li, J., Zhang, L., Dai, B., Xu, J., Zhu, F., Sheng, N., Leung, D.Y.C., 2019. Appl. Catal., B 245, 448–458.
Zhao, W.W., Shan, S., Ma, Z.Y., Wan, L.N., Xu, J.J., Chen, H.Y., 2013. Anal. Chem. 85, 11686–11690.
Zhao, X., Zhou, S., Jiang, L.P., Hou, W., Shen, Q., Zhu, J.J., 2012. Chem. Eur J. 18, 4974–4981.
Zheng, H., Zhang, S., Liu, X., Zhou, Y., Alwarappan, S., 2020. Biosens. Bioelectron. 162, 112234.
Zuo, F., Bozhilov, K., Dillon, R.J., Wang, L., Smith, P., Zhao, X., Bardeen, C., Feng, P., 2012. Angew. Chem. Int. Ed. 51, 6223–6226.
Zuo, F., Wang, L., Wu, T., Zhang, Z.Y., Borchardt, D., Feng, P.Y., 2010. J. Am. Chem. Soc. 132, 11856–11857.